Powder Technology 482 (2026) 122780

Contents lists available at ScienceDirect

Powder Technology

journal homepage: www.journals.elsevier.com/powder-technology

Design and assessment of plowshares for industrial mixers using DEM

Giovanni Bianchi [a],*, Giorgio Tagliavini [b], Andrea Marchetti [b], Gianluca Panzacchi [b], Francesco Braghin [a]

[a] Dipartimento di Meccanica, Politecnico di Milano, Via La Masa 1, Milano, 20156, Italy
[b] WAMGROUP, Via Cavour 338, Ponte Motta/Cavezzo (MO), 41032, Italy

GRAPHICAL ABSTRACT

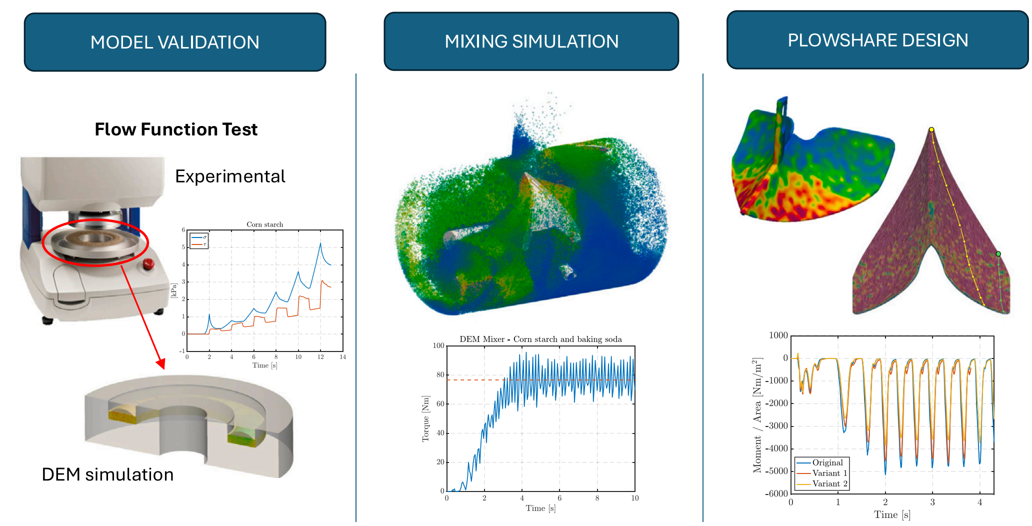

HIGHLIGHTS

- A DEM model for powder mixing was validated using experimental Flow Function Tests.
- Plowshares were designed aiming at maximizing lateral particle transport.
- Improvements in lateral particle transport yield small gains in mixing performance.
- Simulations highlighted a trade-off between mixing performance and required torque.

ARTICLE INFO

Keywords:
Powder mixing
Flow function test
Plowshare design

ABSTRACT

Discrete Element Method (DEM) simulations are increasingly used to analyze powder mixing; however, the design of plowshare geometry in industrial mixers is generally addressed through parametric approaches, with limited insight into the underlying particle transport mechanisms. In this work, a DEM-based framework is developed to analyze plowshare mixer performance by linking plowshare geometry with particle transport mechanisms and mechanical load. DEM material models for baking soda and corn starch are first calibrated and validated against experimental Flow Function Tests, ensuring realistic reproduction of bulk rheology.

* Corresponding author.
E-mail address: giovanni.bianchi@polimi.it (G. Bianchi).

https://doi.org/10.1016/j.powtec.2026.122780
Received 26 November 2025; Received in revised form 23 April 2026; Accepted 3 June 2026
Available online 9 June 2026

The proposed plowshare design strategy focuses on enhancing lateral particle transport, which has been identified as a convective mixing mechanism. Simplified simulations with a single plowshare are employed to isolate geometric effects and compare alternative designs. The proposed plowshare geometry shows enhanced lateral particle redirection in the simplified configuration, confirming the effectiveness of the mechanism-based design approach. Full-scale simulations of the industrial mixer are then performed to assess whether this local transport enhancement translates into improved global mixing performance. The results show that the modified geometry achieves slightly higher Lacey mixing indices and faster mixing evolution, but at the expense of a significant increase in torque demand. These findings demonstrate that improving a local particle transport mechanism does not necessarily lead to a practically advantageous mixer design, and that the overall performance must be evaluated by considering both mixing quality and mechanical load. The proposed framework provides a rational tool for plowshare design and highlights the importance of combining mechanism-based analysis with full-scale validation.

1. Introduction

The mixing of granular materials is a crucial operation in various industrial fields, including food, pharmaceuticals, chemicals, metallurgy, and construction [1–6]. Good mixing ensures a uniform distribution of components in the final product, which determines its chemical and physical properties. In the pharmaceutical industry, it directly influences the therapeutic effect of medicine [4,5]. Therefore, this process must be optimized not only to guarantee its effectiveness but also to minimize its time and energy requirements, which represent a significant fraction of the entire powder production process.

Mixers are generally categorized into rotating vessels (e.g., V-blenders, drums) and fixed vessels with rotating internal elements (e.g., ribbon, plowshare, and plowshare mixers). The latter group relies on convection and shear to promote particle motion and mixing. The optimization of the mixing process involves geometric changes in the mixer and internal equipment, such as plowshares and choppers, as well as adjustments to working conditions, including rotation speed, loading ratio, and mixing time [5]. Such optimization requires a thorough understanding of the underlying physical phenomena involved in powder mixing, which are complex due to the discrete and dissipative nature of granular materials, which are still not fully understood [7]. Granular materials can exhibit arching, segregation, and jamming behaviors, all of which are strongly dependent on parameters like particle shape, size distribution, cohesion, and inter-particle friction [5]. In addition, the coupling between the geometry and dynamics of the mixer makes the characterization and generalization of the mixing process even more difficult [8].

Several experimental and numerical methods were used to investigate powder mixing. Experimental methods involve tracer tracking, such as applying Positron Emission Particle Tracking (PEPT) [9,10] or using X-ray tomography [11], which allows for tracking the complex and three-dimensional motion of dispersed particles without interfering with the mixing process. However, these techniques are expensive, and alternative techniques that rely on image analysis, such as Particle Image Velocimetry (PIV), can be used; however, they can only observe particles on the free surface of the mixing chamber [12].

Conversely, numerical methods offer the possibility to observe the dynamics of the process in great detail. Among these methods, the Discrete Element Method (DEM) enables the simulation of the motion and interactions of each individual particle, which can capture and explain phenomena such as segregation, agglomeration, and particular flow patterns [5]. Several studies have employed DEM to analyze powder mixing, examining the effect of design and process parameters on mixing efficiency. The outcomes of these investigations illustrate the mixing performance of mixers with different geometries such as V-blenders [13,14], tetrapodal blenders [13], revolving static mixers [15], Turbula mixers [10], screw feeders [16,17], conical blenders [5,18], rotating drums [19–21], vertical axis mixers [22], and mixers with rotating blades, or plowshares [1,2,4,12,23,24]. DEM simulations have also been demonstrated to be an effective method for highlighting the effects of different geometries of the plowshares or blades in the mixer on the mixing quality of the powder [4,5,25].

The objective of this research is to examine the mixing performance of an industrial mixer using DEM simulations. The main limitation of DEM simulations is that they require as input the mechanical properties of individual powder particles and the contact forces among them, which are generally unknown. Conversely, the macroscopic behavior of the powder is generally easy to measure using a powder flow tester, which performs the Flow Function Test (FFT). Thus, there is a need to link the macroscopical behavior of the powder to the mechanical properties of the single grains, which can be carried out by creating a DEM simulation of the FFT and the WFT and tuning the particle parameters to obtain the same results obtained experimentally in the simulation [6,26–28]. With a reliable DEM model of different powders, the mixing process in an industrial mixer has been simulated to evaluate the required time and the necessary torque to the plowshare shaft.

Despite the extensive application of DEM to powder mixing systems, a mechanism-oriented design strategy for the plowshare geometry in industrial mixers remains relatively underexplored. Most existing DEM studies focus on optimizing global mixing indices, operating conditions like the rotational speed of the shaft, or plowshare disposition inside the mixer [29], often providing limited insight into how specific geometric features of the plowshare influence particle transport mechanisms and mechanical load. Only a limited number of works have explicitly addressed plowshare geometry optimization using DEM. For instance, Fang et al. [30] investigated the effect of sweep angle on mixing quality by performing multiple simulations and evaluating the resulting mixing index. While such studies provide valuable correlations between geometric parameters and mixing performance, they do not explicitly analyze the particle-scale transport mechanisms responsible for the observed trends, nor do they offer detailed guidance on how to modify blade geometry to enhance specific convective effects while controlling torque demand.

In this work, DEM material models for baking soda and corn starch are calibrated and validated by comparing the results with experimental flow function data, providing a reliable basis for subsequent mixing simulations. The original industrial mixer configuration is then analyzed to quantify torque demand, force distributions, and baseline particle transport behavior. A mechanism-based design strategy is proposed by focusing on lateral particle transport, identified as an important convective mechanism in plowshare mixers. Simplified DEM simulations are used to isolate the effect of plowshare geometry and to assess how specific design modifications influence particle motion. Finally, full-scale simulations of the industrial mixer are performed to directly compare the original and modified plowshare geometries. The extent to which such mechanism-level improvements translate into measurable gains in full-scale mixing performance is explicitly investigated in this work. The results highlight the limitations of transferring local transport enhancements to industrial-scale performance and emphasize the need to consider the trade-off between mixing quality and mechanical load in plowshare design.

The proposed methodology is novel since it combines the calibration of powder behavior from experimental data with a comparative assessment of different plowshare design choices. In addition, the incorporation of customized geometries and assessment of their effect through validated DEM models is a step forward from previous works, which tend to employ simplifying assumptions or generic materials. The paper is organized as follows. Section 2 describes the experimental tests used to characterize the powder and the methods used to calibrate the DEM model; Section 5 presents the mixing simulation results; Section 4 analyzes the performance of different plowshare geometry; finally, Section 6 summarizes the contributions of this work.

2. Materials and methods

Granular materials can be modeled either as discrete assemblies of rigid particles or as continuum-like media. While the Discrete Element Method (DEM) is well-suited for capturing particle-scale dynamics and investigating the influence of microscopic properties such as shape and contact friction, it requires input data regarding the mechanical properties of the individual particles, which are difficult to measure directly and are strongly dependent on the specific powder sample used [28]. Conversely, continuum models describe the material behavior using bulk properties such as cohesion, internal friction angle, and wall friction, which are more easily obtained experimentally from standard rheological tests. The most commonly constitutive law used to describe yielding in granular materials is the Mohr–Coulomb failure criterion, which relates normal σ and shear stresses τ via material-dependent cohesion c and internal friction angle ϕ [31].

$$\tau = c + \sigma \tan\phi \tag{1}$$

These parameters are influenced by environmental conditions such as humidity and compaction history, and can be experimentally determined using a shear cell test or ring shear tester [32]. In this study, the macroscopical mechanical behavior of the powders was characterized using the Brookfield Powder Flow Tester, following ASTM standards D6773 [33], D6682 [34], and D6128 [35]. This device features a hollow ring, which is filled with powder and covered by a rotating lid. The machine compresses and rotates the lid to generate a normal force N and a torsional moment M_t, which are measured by load cells. The normal and tangential stresses are computed with simple geometrical considerations:

$$\sigma = \frac{N}{\pi\left(R_e^2 - R_i^2\right)} \tag{2}$$

$$\tau = \frac{3M_t}{2\pi\left(R_e^3 - R_i^3\right)} \tag{3}$$

The device performs both Flow Function Tests (FFT) to determine the unconfined yield strength as a function of consolidation stress and Wall Friction Tests (WFT) to evaluate the wall friction angle. From the FFT data, the flow function index was computed as follows [31]:

$$ff_c = \frac{\sigma_1}{\sigma_c}, \tag{4}$$

where σ_1 is the major principal consolidation stress and σ_c is the unconfined yield strength [31].

Although DEM does not use bulk properties directly, the DEM model can be calibrated by simulating these rheological tests and tuning microscopic parameters, such as particle friction, rolling resistance, restitution, and stiffness, until the simulated results align with experimental observations. This indirect calibration strategy is widely used to ensure consistency between simulations and the real bulk behavior of granular media [6,26,28].

2.1. Calibration of the DEM parameters

To reproduce the macroscopic behavior of granular materials in DEM simulations, a systematic sensitivity analysis was conducted to understand how each particle-level parameter affects bulk properties, including cohesion, internal friction angle, wall friction angle, bulk density, and viscosity. The calibrated parameters include:

- Young's modulus E: it primarily affects contact stiffness and numerical stability, with limited influence on quasi-static bulk behavior [36–39];
- Poisson's ratio ν: it has negligible influence on bulk behavior and was fixed to a standard value equal to 0.3 [38];
- coefficient of restitution CoR: it affects energy loss and material resistance to flow, especially for materials with high friction [31, 40,41];
- static friction coefficient μ_s: it has a strong influence on internal friction angle and shear resistance of the granular assembly and was therefore identified as one of the most influential parameters governing bulk rheological behavior and bulk density [31,36,42];
- rolling resistance coefficient C_{rr}: it accounts for particle resistance to angular displacement and contributes to bulk shear strength and packing behavior, particularly at higher friction levels [36, 43];
- particle shape: it is represented using clumped spheres to reproduce the low packing density and high shear resistance observed experimentally on particles with irregular geometry [42,44];
- particle dimension: it was scaled to reduce computational cost while preserving the relevant flow and force transmission mechanisms [39], ensuring that particle dimensions remained small relative to the characteristic geometric features of the mixer.

A complete list of calibrated DEM parameters for each material is reported in Appendix A, while a detailed sensitivity analysis supporting parameter selection is reported in the Supplementary Material. Considering the effect of every particle-level input parameter, the primary objective of this work is to develop DEM simulations of various powders that accurately reproduce both the macroscopic rheology and interaction forces measured experimentally during Flow Function Tests. This calibration strategy provides confidence that the simulated particle dynamics and force transmission mechanisms observed in the mixer simulations are physically meaningful and not artifacts of arbitrary parameter selection. The validated DEM models are therefore suitable for analyzing the influence of mixer geometry on particle transport mechanisms and mechanical load.

2.2. Numerical implementation

The software used to perform this numerical analysis is DEM-Engine, a submodule of Project Chrono specifically designed for DEM simulations [44]. The main advantage of DEM-Engine is its computational efficiency, as it utilizes two parallel threads: one to update the contacts among particles and another to integrate the motion equations, which can be executed on two different GPUs. The simulation can include granular particles and rigid bodies. DEM-Engine allows not only the defining of the material characteristics but also the shape of the particles, which is defined as a clump of partially overlapped spheres with different diameters [44]. Rigid bodies are defined as meshes created with separate software and imported.

3. Validation of DEM model

The two materials used in this study are baking soda and corn starch, which are common ingredients in the food industry.

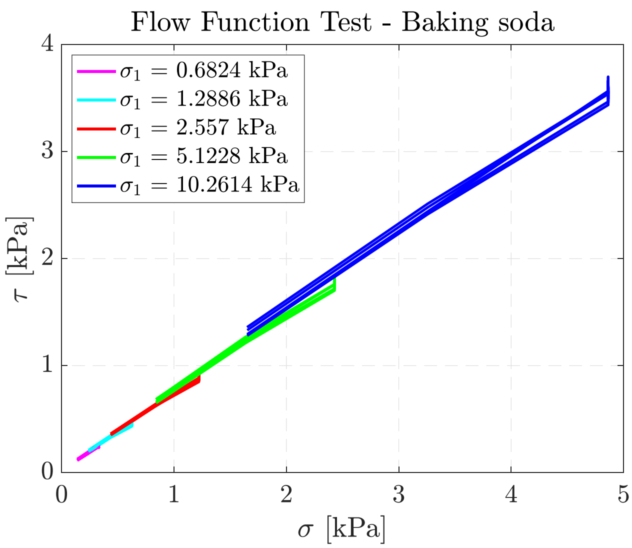

Fig. 1. Flow Function Test of baking soda.

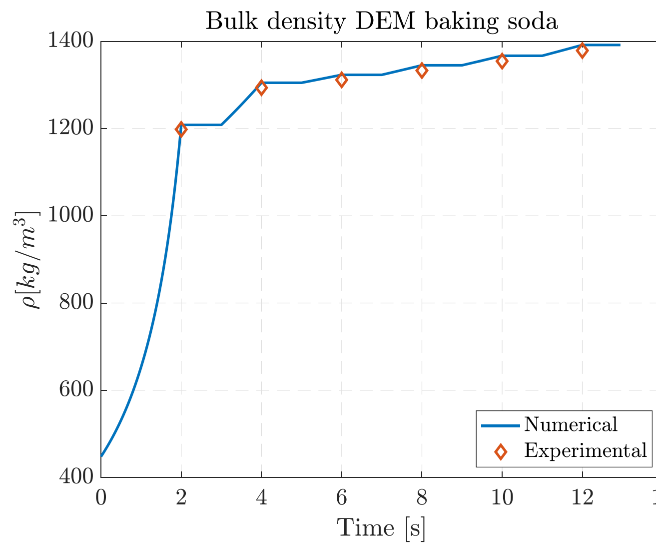

Fig. 2. Bulk density of baking soda during the FFT.

Table 1
Baking soda rheological characteristics.

Cohesion c	Internal friction angle ϕ
0.0212 kPa	37.64°

3.1. Baking soda validation

The particles of baking soda have an irregular shape, and the particle density is 2160 kg/m^3. The sieve size of the particles is listed in the supplementary materials, and the average particle dimension is 138.37 μm.

The result of the FFT is shown in Fig. 1, where the normal and tangential stresses are measured for different consolidation stresses σ_1.

The yield limit curves plotted at different consolidation stresses are very similar to straight lines and almost overlap, which indicates that the Mohr–Coulomb criterion is valid for baking soda and that both the internal friction angle and the cohesion can be considered independent of the consolidation stress σ_1 without introducing significant error. The outcomes of this test are listed in Table 1.

To shorten the simulation time, the lid movement in the DEM simulation has been simplified as a sequence of compressions followed by rotations, neglecting the consolidation stress release and reapplication each time. The vertical displacement of the lid was obtained from the experimental measurements of bulk density, whereas the angular displacement could not be extracted from the experimental data. However, it is sufficient for the latter to exceed the displacement required to induce material yielding, and it was therefore determined by trial and error. Since, at the very low velocities considered, the stresses do not depend on particle velocity, the angular velocity of the lid was increased to shorten the simulation time, and both the compression and shear phases were set to last 2 s each.

The characteristics of baking soda found after the calibration of the model are listed in Table A.6. The wall friction coefficient μ_w has been measured experimentally with a Wall Friction Test.

During the first two seconds of the simulation, the particles fall from their initial position. This is necessary because DEM-Engine uses the Hexagonal Close Packing (HCP) algorithm to initialize particle placement without initial contacts. The actual test begins at t = 2 s, when the lid closes the chamber.

In Fig. 2, the bulk density obtained with the DEM simulation at different compression stages is presented and compared with the one obtained experimentally, which is very accurately reproduced.

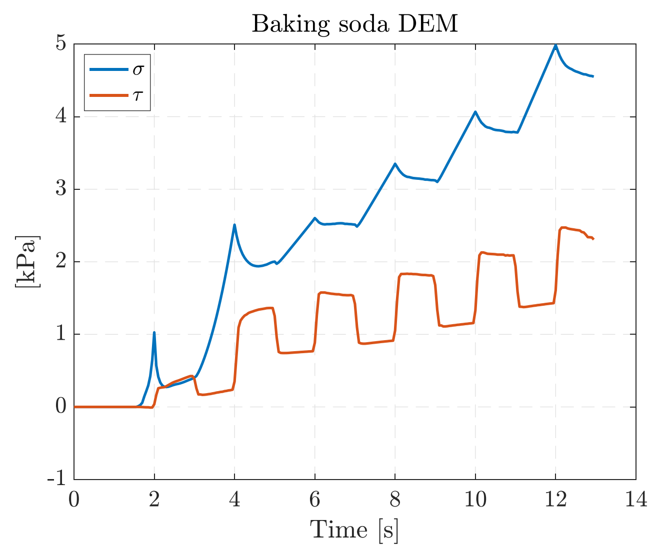

Fig. 3. Stresses on baking soda during the FFT.

Normal and shear stresses are shown in Fig. 3. During the compression phases, the normal stresses increase linearly, whereas the shear stresses remain constant. Instead, during the rotation phases, the normal stresses slightly decrease since the shear stresses cause particle rearrangement, and some particles fill the voids, packing the material more densely. At the beginning of the rotation phase, the shear stresses increase linearly as the angular displacement increases; then, after yielding, they remain constant.

The compressive stresses during the first two stages are proportionally much higher than those observed in the subsequent stages. This is due to the fact that, in the first two stages, the vertical displacement of the lid is greater. Since the material exhibits low flowability and high friction coefficients, the particles tend to compress rather than move to fill the voids. When the material is forced to move due to the applied torsion, it fills the empty spaces, and the compressive stress decreases significantly. From the third stage onward, this effect becomes much less pronounced, both because the vertical displacement of the lid is reduced and because the material has already undergone two compression and torsion cycles, leaving fewer voids to fill.

Fig. 4 shows the stress states on the $\sigma - \tau$ plane for the baking soda during the Flow Function Test, compared with the experimental

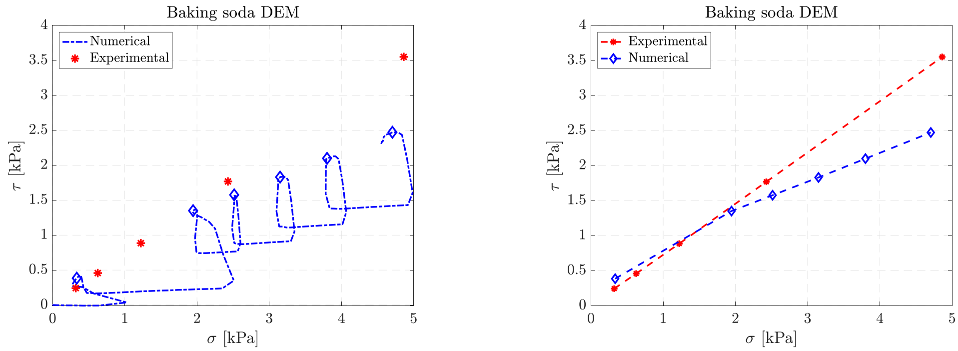

(a) Stresses during the FFT (b) Yield limit of the baking soda

Fig. 4. DEM simulation of the FFT with baking soda.

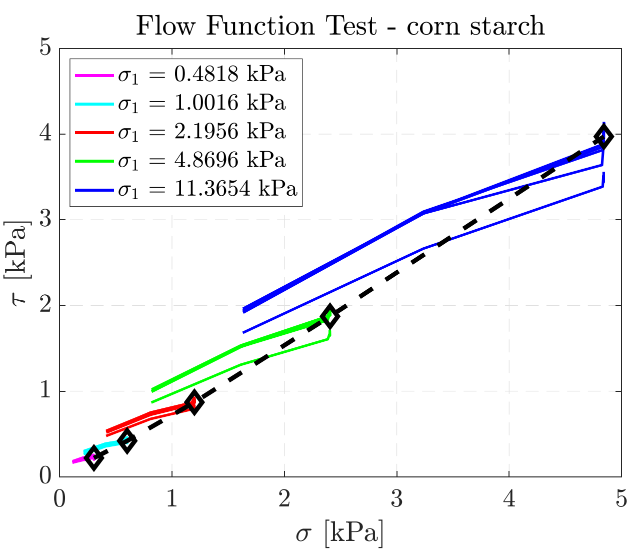

Fig. 5. Flow Function Test of corn starch.

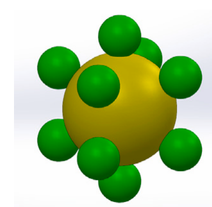

Fig. 6. Corn starch particle.

Table 2
Corn starch rheological characteristics.

Cohesion c	Internal friction angle ϕ
0.4339 kPa	23.71°

data. Regarding the experimental results, only the points at the end of each phase are highlighted, which correspond to the yield limit of the material and which are the only ones made available by the testing machine. For the simulation results, all stress states are shown, with those corresponding to the yield limit highlighted with diamonds.

The points exhibiting the largest discrepancies are those computed under lower consolidation stresses, as they are strongly influenced by the initial conditions. During the early stages of the test, the particles are still arranged in a highly ordered configuration, and in certain regions, they are almost vertically aligned. This strong dependence on the initial arrangement is also reflected in the experimental data, where the position of these points on the stress plane varies significantly from one test to another. However, since the particles are always randomly arranged in the experimental tests, the corresponding stresses tend to be lower than those obtained numerically. Conversely, the points at higher stress levels are reasonably close to the experimental results. Although the numerical and experimental yield points do not coincide exactly, they lie along the same line. Therefore, it can be concluded that the granular material model used in these simulations accurately reproduces the constitutive behavior of baking soda.

3.2. Corn starch validation

Cornstarch particles have an irregular shape, and their dimensions depend on the process used to extract them from corn kernels. The sieve size of the particles is listed in the supplementary materials, and the average particle dimension is 187.78 μm. The density of each particle is $1450\,kg/m^3$.

Fig. 5 shows the result of the Flow Function Test, i.e., the yield limit of the material at different consolidation stresses σ_1. As can be observed, the yield limit increases with increasing consolidation stress. The Mohr–Coulomb criterion is also applicable to corn starch, as the yield limit curves can be approximated by straight lines. However, assuming that the friction angle ϕ and cohesion stress c are independent of the consolidation stress σ_1 leads to an inaccurate representation of the material behavior. Nevertheless, reproducing the complete viscometer cycle entails a prohibitively high computational cost, as it would require repeating a cycle of compressions and rotations for each consolidation stress level, with each cycle preceded by an initial compression and rotation to reach the pre-shear stress condition. Therefore, the DEM model of corn starch was calibrated to simulate only the points highlighted in black in Fig. 5. This approach slightly underestimates the maximum shear stress the material under low compressive stress that follows a precompression, a condition not typically encountered in a mixing process.

The outcomes of the FFT with corn starch are listed in Table 2.

The vertical movement of the lid was calculated with the same criterion used for the baking soda, and the characteristics of corn starch found after the calibration of the model are listed in Table A.7. The wall friction coefficient μ_w has been measured experimentally with a Wall Friction Test.

The solid fraction of uncompressed corn starch is 34%, and this characteristic could not be reproduced using spherical particles. Therefore, it was necessary to model the particles with a more complex shape, shown in Fig. 6. Each particle consists of a central sphere and ten smaller spheres arranged on its outer surface. The diameter ratio between the smaller spheres and the central one is 3/8, while the

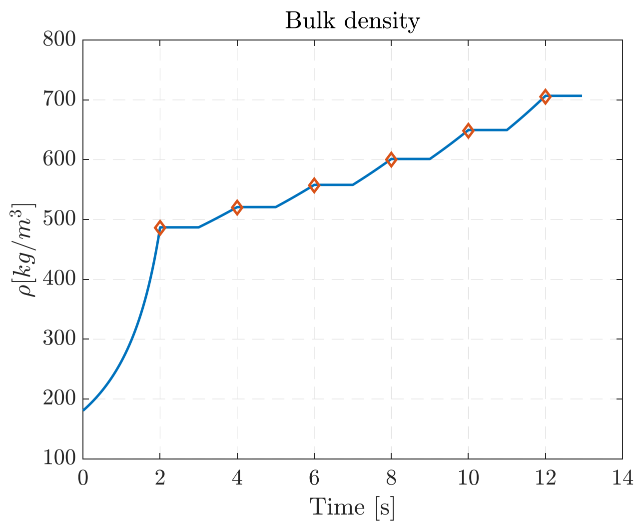

Fig. 7. Bulk density of corn starch during the FFT.

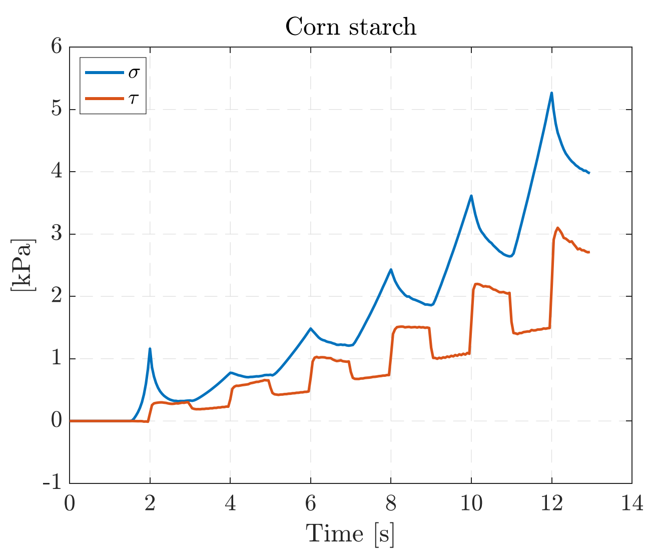

Fig. 8. Stresses on corn starch during the FFT.

centers of the small spheres lie on an imaginary sphere with a radius equal to 13/10 of the central sphere. The distance between the two farthest points of the small spheres is 1.7 mm.

In Fig. 7, the bulk density of the corn starch sample is shown, and it is possible to note that the simulation reproduces very accurately the bulk density of the material, recreating the void spaces present in the sample.

The normal and shear stresses are shown in Fig. 8. During the compression phases, the normal stress σ increases with the downward displacement of the lid. Shear stresses τ also increase, but less significantly. During the torsion phase, the normal stress decreases as particles rearrange and fill the voids, compacting the material. Meanwhile, the shear stresses increase linearly as long as the material remains compact. Once yielding occurs, the shear stresses remain approximately constant or slightly decrease due to the continued filling of voids.

Fig. 9 shows the stress states on the $\sigma - \tau$ plane for corn starch during the Flow Function Test, compared to the experimental results. For the experimental data, only the points at the end of each phase are highlighted, corresponding to the yield limit of the material. In contrast, for the simulation results, all stress states are shown, with the yield limit points also highlighted. The points showing the most significant discrepancies are those computed at higher consolidation stresses, as pre-shear stresses were not applied in the simulation to compact the material. As a result, the uncompressed material exhibits a lower shear strength. Nevertheless, the lines representing the yield limit of corn starch found in the experiments and with the DEM simulation present a high level of overlap.

3.3. *Angle of repose*

In addition to the FFT calibration, the DEM material models were further assessed by simulating the angle of repose of both materials. The simulations involved 49666 particles, which were allowed to fall through a funnel and form a granular pile. The final configuration is shown in Fig. 10, while a complete animation is provided in the supplementary materials. The angle of repose of baking soda reported in the literature spans a wide range, typically between 19° and 46°, depending on moisture content and processing conditions [45,46]. The DEM model predicts an angle of 38°, which lies within the upper half of the reported range and is consistent with moderately cohesive conditions. Similarly, the angle of repose of corn starch is usually reported between 45° and 56°, with significant variability due to particle size and moisture [47–50]. The value obtained in this study, 46°, is close to the lower bound of the range and is consistent with relatively free-flowing powder conditions. Although the literature values exhibit substantial variability, the DEM predictions fall within physically meaningful ranges and reflect the chosen material parameters. The angle of repose is therefore used here as a consistency check of the bulk flow behavior rather than as a strict validation metric. This result supports the suitability of the adopted DEM parameters for simulating the mixing process.

4. Mechanism-oriented design of the plowshare geometry

The plowshare is the key component of the mixer, responsible for pushing particles forward and outward, inducing both tangential and axial motion, and enabling convective mixing [23]. The mixing performance depends on several parameters, including the number of plowshares, their axial spacing, the rotational speed of the shaft, the fill level of the mixer, and the shape of the plowshares themselves [23,30], in particular the sweep angle γ, which allows the best mixing for values around 35° [30]. The objective of this study is to investigate how specific plowshare geometries influence lateral particle transport under controlled conditions, which represents a key convective mechanism contributing to powder mixing in plowshare mixers, without increasing the required torque on the shaft. To this end, several plowshare designs were proposed and compared through DEM simulations. To allow the comparison of a large number of geometries while keeping computational costs acceptable, the simulation setup was simplified. A single plowshare was placed inside a cylindrical chamber, and only baking soda particles were used. Since the analysis focuses on the geometric contribution of a single plowshare, a simplified configuration was adopted to isolate lateral redirection mechanisms. In this context, lateral particle displacement is employed as a qualitative and comparative indicator of convective mixing potential rather than as a direct measure of global mixing quality. All the simulations involved a single plowshare rotating in a cylinder with a radius of 250 mm and a height of 400 mm. The plowshare started from rest and accelerated at a constant rate of 9.4248 rad/s^2 for 2 s, then rotated at a constant speed of 18.8496 rad/s (180 rpm). In these simulations, the baking soda particles are positioned at the top of the chamber to prevent initial overlap with the plowshare, and as the simulation begins, they fall under the influence of gravity.

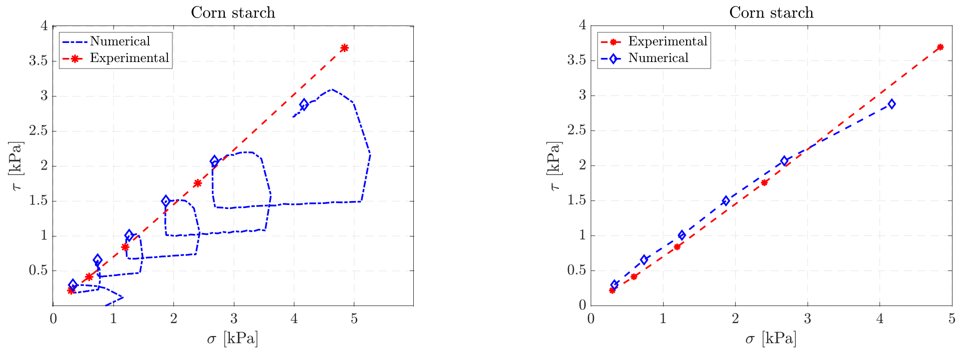

(a) Stresses during the FFT
(b) Yield limit of the corn starch

Fig. 9. DEM simulation of the FFT with corn starch.

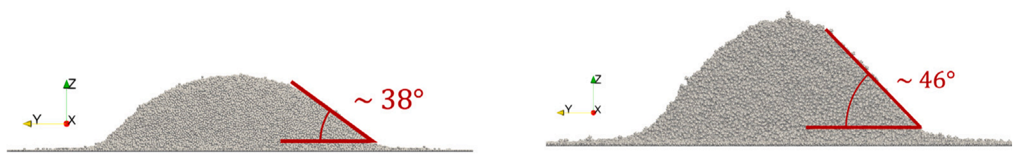

(a) Angle of repose of baking soda
(b) Angle of repose of corn starch

Fig. 10. Angle of repose of baking soda and corn starch.

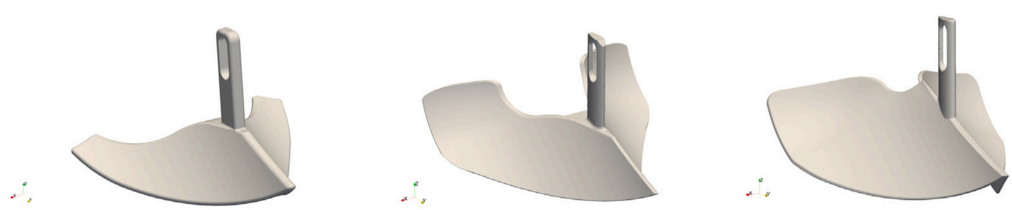

(a) Original ($\gamma = 27°$)
(b) Variant 1 ($\gamma = 29°$)
(c) Variant 2 ($\gamma = 27°$)

Fig. 11. Geometries of the different plowshares analyzed.

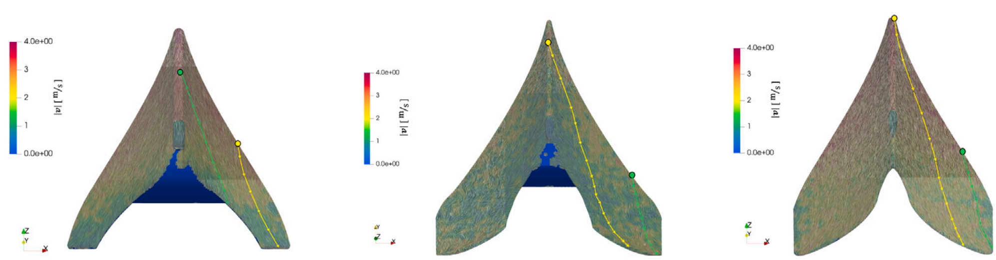

(a) Original
(b) Variant 1
(c) Variant 2

Fig. 12. Trajectory of the particles on the plowshares' surface.

4.1. Plowshare geometry

The working principle of a plowshare is to lift particles from the chamber bottom and push most of them laterally, leaving a void behind, which is filled by particles that fall back under gravity. Fig. 11 shows the modifications that have been made to the original plowshares geometry to enhance the lateral particle displacement.

In the first plowshare variant, the cross-section of the shaft connecting the plowshare to the central axis has been redesigned, changing it from a rectangular to an aerodynamic profile to reduce drag. Then, two terminal lobes have been incorporated at the trailing edge of the plowshare to prevent particles from falling behind and, instead, deflect them sideways. The second plowshare variant maintains the terminal lobes introduced in variant 1, although they extend more inward and less outward, and the inclined surface of the plowshare is prolonged behind the shaft to prevent particles from falling behind rather than being pushed laterally.

4.2. Particle motion and lateral transport mechanisms

Fig. 12 compares the particle velocity fields induced by the original plowshare and the two modified geometries at identical operating conditions and shaft position. As shown in Fig. 12(a), some particles, such as the yellow one, are successfully deflected sideways, whereas others, like the green one, are redirected to the rear, limiting lateral mixing. As a consequence, a fraction of particles can flow beneath or behind

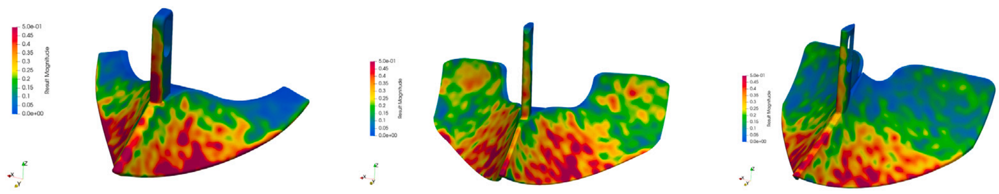

(a) Original (b) Variant 1 (c) Variant 2

Fig. 13. Comparison of the absolute value of the contact forces acting on different plowshares.

Table 3
Maximum values of torque and lateral force for the different plowshares.

	Moment	Moment/Area	Moment/Width	Force	Force/Moment
Original	89.7 Nm	5133 Nm/m^2	354.0 Nm/m	387.3 N	4.45 N/Nm
Variant 1	103.6 Nm	4610 Nm/m^2	374.0 Nm/m	450.9 N	4.51 N/Nm
Variant 2	94.9 Nm	3834 Nm/m^2	374.4 Nm/m	458.2 N	4.95 N/Nm

the plowshare, resulting in a narrower lateral redistribution region. Moreover, the support rod's flat shape interrupts the particle flow and generates resistance without significantly contributing to mixing, so its removal is advised.

The introduction of trailing lobes in Variant 1 significantly alters particle trajectories, preventing particles from falling behind and, instead, deflecting them sideways, as shown in Fig. 12(b), creating a deep furrow. However, many particles located behind the plowshare tend to fall downward, filling the void left behind, similar to what was observed with the original plowshare. Since this plowshare redirects nearly all the particles laterally, with almost none exiting from the rear, the particles that fall behind the plowshare are not those displaced during the current pass, as it occurred with the original design, but rather particles located deeper inside the chamber that were not engaged during this rotation. Therefore, this phenomenon does not represent a significant drawback, as those particles will be displaced in the next cycle. However, it remains an aspect that could be improved, as the upper rear portion of the plowshare, located behind the support rod, currently does not contribute significantly to particle movement.

Fig. 12(c) shows how Variant 2 further modifies the particle motion pattern, deflecting and ejecting all the particles in contact with the front and central parts laterally, such as the yellow particle, whereas some particles, already located at the sides, such as the green one, are not further deflected. The extension of the inclined rear surface beyond the support rod intercepts particles located above the rear region of the plowshare, preventing them from falling back into the void generated by the plowshare passage. As a result, particles are more consistently redirected laterally, and the resulting redistribution region is both wider and more homogeneous compared to the original geometry and Variant 1, despite having approximately the same dimensions. This improvement in lateral displacement of particles is mainly due to the absence of particles directly above the rear portion of the plowshare, as they were displaced laterally during the previous rotation. Furthermore, the cylindrical surface at the bottom of the plowshare was removed since it did not come into contact with the particles. These observations indicate that the geometric modifications progressively shift the dominant transport mechanism from predominantly forward displacement toward lateral convective redistribution, with Variant 2 exhibiting the most effective lateral particle displacement.

4.3. Distribution of contact forces on the plowshare surfaces

The differences observed in particle motion are reflected in the spatial distribution of contact forces acting on the plowshare surfaces. Fig. 13 compares the magnitude of the contact forces at the most loaded shaft position, which occurs when the plowshare is at the bottom of the chamber. For the original plowshare, the highest force concentrations are localized on the front and central regions, while the rear portion contributes marginally to particle redirection. This force distribution is consistent with the limited lateral transport observed in the particle velocity fields. In Variant 1, the addition of trailing lobes introduces significant force contributions on the lateral extensions. These regions actively prevent particle backflow and promote lateral displacement, but their outward location increases the effective moment arm of the resulting forces. Variant 2 exhibits higher forces in the central and front regions, and a rear section less loaded but still contributing to lateral redirection. The lobes predominantly push particles forward, with a less pronounced lateral component, particularly at their outer tips, although a lateral force is still present. This configuration indicates that lateral redirection is achieved through more efficient particle interception rather than increased lever arm, contributing to improved mechanical efficiency.

4.4. Comparison of torque and lateral force metrics

The observations discussed above are supported by quantitative force and torque metrics. Table 3 reports the maximum values of torques and lateral forces obtained for different plowshares, which are obtained at the time instant when the plowshare is at the bottom of the chamber. Peak values of torque and force are reported rather than time-averaged values since these last are strongly influenced by the fraction of time the plowshare is fully immersed in the granular bed, which depends on instantaneous local packing and may therefore introduce a bias dependent on how full the chamber is. Peak values, instead, consistently correspond to the fully immersed condition for all geometries and are thus more representative of the intrinsic mechanical demand and force transmission of each design. The complete time evolution of forces and moments is provided in the supplementary material.

Variant 1 differs from the original plowshare only through the addition of side ears, which increase both the area and the width of the plowshare, significantly enhancing lateral displacement while incurring a moderate increase in torque. The torque increase in Variant 1 is less than proportional to the size increase, making it a more efficient design than the original. In contrast, Variant 2 exhibits a torque demand only marginally higher than the original geometry. This increase is modest due to the fact that the lobes are extended inward rather than outward as in Variant 1. Thus, most of the additional surface area is located in the upper part of the plowshare, which effectively contributes to the lateral redirection of particles but does not significantly increase the required torque since the force application point is closer to the axis of rotation. Moreover, to directly quantify lateral transport efficiency, the lateral force component acting on the plowshares is reported together with the ratio between lateral force and torque. This comparison

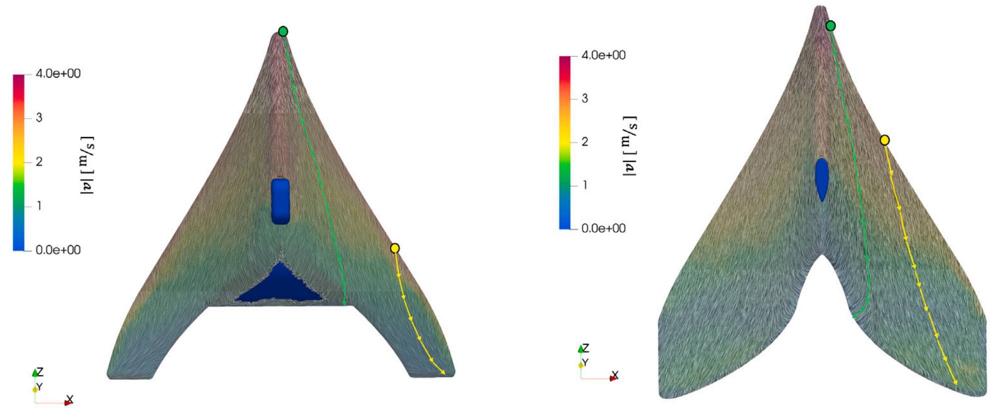

(a) Original (b) Variant 2

Fig. 14. Streamlines of corn starch particles on different plowshares.

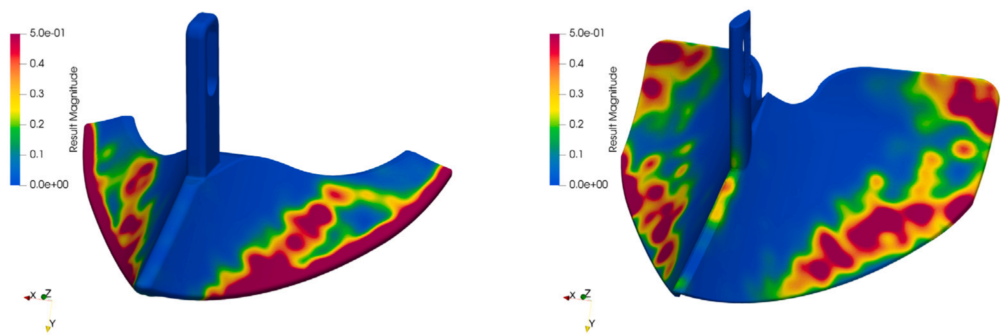

(a) Original (b) Variant 2

Fig. 15. Comparison of the absolute value of the contact forces acting on different plowshares with corn starch particles.

demonstrates that Variant 2 provides the most efficient conversion of mechanical input into lateral convective transport, confirming its superior performance among the investigated geometries.

4.5. Interpretation of geometric effects

The comparative analysis allows identifying clear relationships between specific geometric features and performance indicators. The introduction of trailing lobes consistently reduces particle backflow and increases lateral force generation, while the extension of the rear inclined surface improves particle interception above the plowshare, leading to more homogeneous lateral redistribution. At the same time, the radial position of these geometric features strongly affects torque demand. Outward extensions increase the force lever arm and lead to higher torque, as observed for Variant 1, whereas inward redistribution of the lobes in Variant 2 maintains the force application closer to the shaft axis, limiting torque increase while preserving lateral transport efficiency. Table 4 provides a systematic interpretation of the results by explicitly linking geometric features to particle transport mechanisms and performance indicators.

These observations demonstrate that plowshare performance is governed by a balance between particle interception efficiency and force application distance, providing practical design guidelines that can be generalized beyond the specific geometries investigated.

4.6. Evaluation of the plowshare performances with different materials

To evaluate the influence of material properties on the effectiveness of the proposed plowshare geometry, additional simulations were performed using corn starch. Compared to baking soda, corn starch exhibits higher cohesion and irregular particle shape, which generally reduce particle mobility and lateral redistribution.

Table 4
Qualitative relationship between key geometric features of the investigated plowshares, the resulting particle transport mechanisms, and the observed performance indicators.

	Original	Variant 1	Variant 2
Trailing lobes	Absent	Present (outward)	Present (inward)
Rear inclined surface	Limited	Limited	Extended beyond support
Force lever arm	Baseline	Increased	Comparable to baseline
Resulting performance	Limited lateral transport, lowest force generation	Higher lateral force, increased torque demand	Enhanced lateral transport with moderate torque increase

Fig. 14 compares the particle velocity fields obtained with the original plowshare and the Variant 2 geometry under identical operating conditions. Overall, lateral particle transport is less pronounced than in the baking soda case, reflecting the reduced flowability of the material. Nevertheless, Variant 2 consistently promotes a broader and more coherent lateral redistribution of particles compared to the original design.

The same qualitative trend is observed in the force distributions acting on the plowshares. Fig. 15 shows that, despite the increased

Table 5
Maximum values of torque and lateral force for the different plowshares with corn starch particles.

	Moment	Moment/Area	Moment/Width	Force	Force/Moment
Original	108.4 Nm	6204 Nm/m^2	427.8 Nm/m	115.6 N	3.87 N/Nm
Variant 2	77.26 Nm	3834 Nm/m^2	304.7 Nm/m	91.0 N	3.18 N/Nm

resistance associated with corn starch, Variant 2 generates higher lateral force components than the original plowshare, indicating enhanced particle interception and redirection.

A quantitative comparison of normalized force and torque indicators is reported in Table 5. Although Variant 2 exhibits lower force and torque levels at steady state compared to the original design, this behavior does not indicate reduced effectiveness. On the contrary, it reflects the higher efficiency of lateral particle transport achieved during the initial passes. For cohesive materials such as corn starch, particles displaced laterally by Variant 2 plowshare do not readily flow back toward the center of the mixer. As a result, once a furrow is formed, the plowshare encounters fewer particles in subsequent rotations, leading to reduced forces and torque in subsequent rotations. In contrast, the original plowshare promotes weaker lateral redistribution, causing particles to repeatedly enter back the central region and resulting in sustained mechanical loading over multiple rotations. This behavior can be observed in the animations provided as Supplementary Materials and from the time evolution of forces and torques shown in the Supplementary Materials. While absolute values differ from those obtained with baking soda, the relative performance ranking of the geometries remains unchanged: Variant 2 achieves more effective lateral particle transport with reduced steady-state force and torque levels compared to the original design. These results indicate that, although material properties strongly affect the absolute magnitude of particle motion and forces, the geometric mechanisms underlying the optimized plowshare remain effective for materials with markedly different cohesion and shape characteristics.

5. Simulation of the full-scale industrial mixing process

After validating the material models and designing the plowshare based on the particle transport mechanism, the full-scale industrial mixing process was simulated to rigorously evaluate whether the modified plowshare geometry yields a measurable improvement in mixing performance. Validation of the DEM simulation parameters was conducted with the original plowshare, while comparative assessments between geometries were subsequently carried out through dedicated full-scale simulations. The primary metrics analyzed in this study include mixing quality, as quantified by the Lacey index, and the torque exerted on the mixer shaft. The shape of the particles and the mechanical properties of the constituent materials exert a pronounced influence on both the loading experienced by the plowshares and the achieved mixing quality. Accordingly, it is essential to employ particle shapes validated via shear cell simulations. In the case computational costs become prohibitive, an increase in particle size may be adopted to reduce simulation time, as suggested in [29].

The mixer used in the simulation is shown in Fig. 16. To start from a realistic initial condition, a hopper was added to the mixer, allowing the particles to enter through the top opening and settle randomly on the bottom surface. The mixer chamber is a cylinder with a 250 mm radius and an axial length of 780 mm.

The materials employed in the mixing simulations correspond to those previously validated, specifically corn starch and baking soda. In the comparative full-scale simulations, both materials were modeled as particles with identical radii (2 mm) and were introduced at equivalent volume fractions.

The torque on the shaft was also used as a parameter to validate the sensitivity of the simulation to the grain size. Fig. 17 shows a comparison between the torque on the shaft obtained using particles with a radius of 1.5 mm, 2 mm, and 5 mm. In the simulation with 5 mm particles, the transient phase is significantly longer because the particles take much longer to fall from the hopper into the mixing chamber. Furthermore, even in the steady state, some differences can be observed: the torque resulting from the 5 mm particles is considerably less regular. Given the pronounced effects of particle size

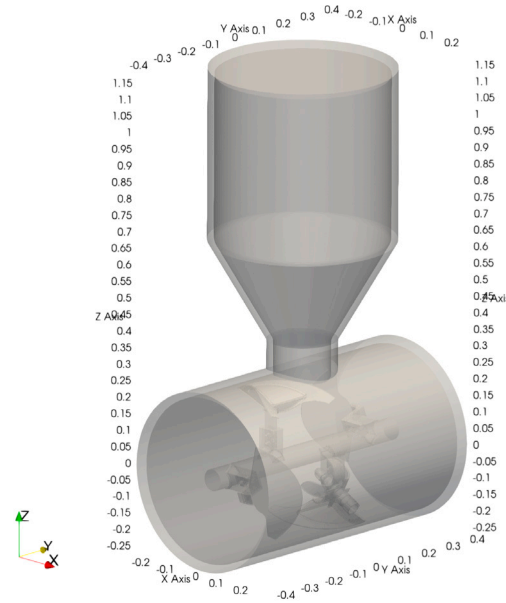

Fig. 16. Mixer with hopper.

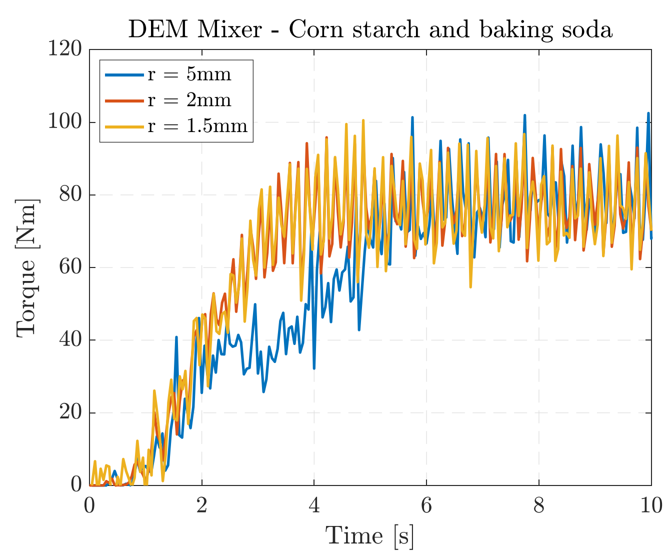

Fig. 17. Comparison of the results with different particle sizes.

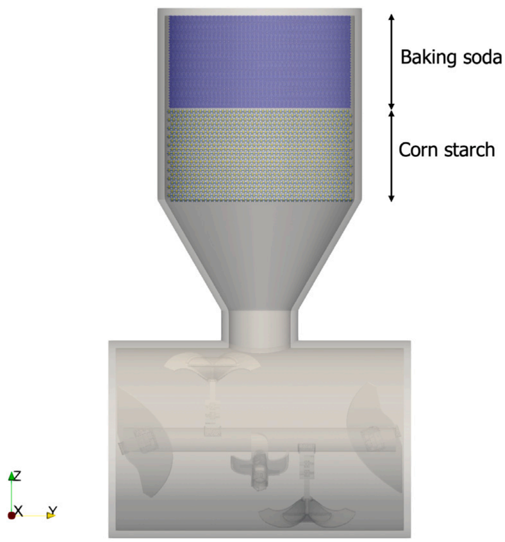

Fig. 18. Initial condition of the particles in the mixer.

scaling, the simulation with 5 mm particles was discarded. On the other side, the torques obtained with particles of 1.5 mm and 2 mm are almost identical, meaning that the 2 mm particle simulation does not suffer from similar scaling issues. The particle size was selected to balance numerical efficiency and physical fidelity, while ensuring that particles remain sufficiently small relative to the characteristic geometric features of the mixer and plowshares. This indicates that, below a critical particle size threshold, the simulated mixing dynamics become effectively independent of particle size. This behavior suggests that shear forces, force transmission to the plowshares, and particle rearrangement mechanisms are primarily governed by collective interactions and bulk rheology rather than by absolute particle size. This is particularly relevant for non-spherical particles such as corn starch, where angularity and contact multiplicity dominate shear resistance and mixing behavior. The observed independence of segregation and mixing kinetics from particle size for sufficiently small particles supports the validity of the chosen scaling factor and indicates that segregation and mixing kinetics are not influenced by particle size within the investigated range.

The mixer was loaded with 15.44 kg of corn starch and 22.15 kg of baking soda, corresponding to occupied volumes of $10.65 \times 10^{-3}\mathrm{m}^3$ and $10.25{\times}10^{-3}\mathrm{m}^3$, respectively. Consequently, the mixture is composed of approximately equal volume fractions of each material. Considering only the actual volume occupied by the particles (excluding interstitial voids), the fill level of the mixer is 14%. If the bulk volume, including inter-particle voids, is considered, the fill level increases to 33%. This moderate fill level aligns with the computational constraints of DEM modeling and the necessity of retaining the hopper in the simulation setup. Although the granular materials occupy only a fraction of the total mixer volume, the configuration is sufficiently representative for comparing the two plowshare geometries under identical operating conditions. Fig. 18 shows the distribution of corn starch and baking soda particles at the initial time frame of the simulation.

The mixer consists of a shaft with two plowshares mounted at 180° out of phase and two scrapers at the sides. Moreover, there is a chopper in the middle. The mixer shaft starts from rest, and for the first 2 s, it accelerates with a constant angular acceleration of 9.4248 $\mathrm{rad/s^2}$, then it rotates at a constant angular velocity of 18.8496 rad/s, i.e., 180 rpm. The chopper also starts from rest and accelerates for the first 2 s with a constant angular acceleration of 78.54 $\mathrm{rad/s^2}$, then rotates at a constant angular velocity of 157.08 rad/s, i.e., 1500 rpm.

Fig. 19 shows the mixer from two different angles, highlighting that the particles in proximity to the plowshares and scrapers exhibit very high velocities, whereas those located farther from these elements are nearly stationary. However, since the plowshares and scrapers extend along the entire length of the cylinder's axis, the particles that are stationary at a given instant are in motion when the shaft reaches a different position and vice versa. As a result, there are no stagnant regions within the mixer where the powder remains unmixed. The plowshares push the particles in front of them forward and outward, while the voids left behind are filled by adjacent particles moving inward. The scrapers displace the particles along the cylinder walls forward and inward, causing them to fall back into the region where the plowshares operate, thereby enhancing the overall mixing process.

The forces acting on the plowshares and scrapers are shown in Fig. 20. The plowshares and scrapers experience the highest loads when located at the bottom of the mixer, as this is where the most significant quantity of powder is displaced, and their entire surface is in contact with the material. When positioned on the lateral sides, they are subjected to intermediate forces, which are comparable during both the upward and downward motion. In the upward phase, the plowshares lift the particles against gravity, while in the downward phase, they must penetrate the material, overcoming frictional resistance. Conversely, when they are at the top of the mixer, they are almost entirely free from mechanical loads.

5.1. Comparison of plowshare geometries' performance

At steady state, the average torque required to rotate the shaft supporting the plowshares and scrapers is approximately 90 Nm for the original plowshare geometry and 107 Nm for the modified design. As shown in Fig. 21, the transient phase lasts longer than the 2 s required

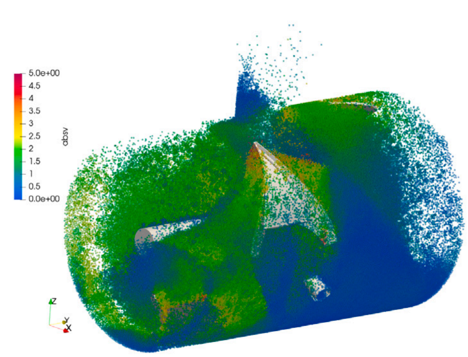

(a) Front view

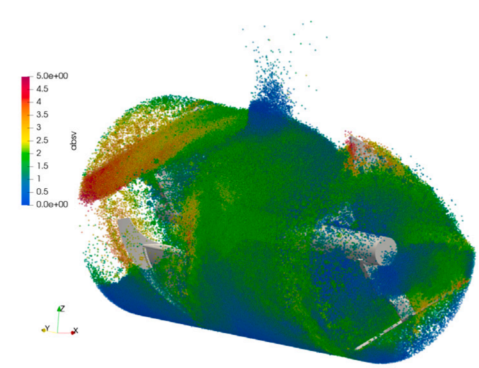

(b) Back view

Fig. 19. Particle velocity in the mixer.

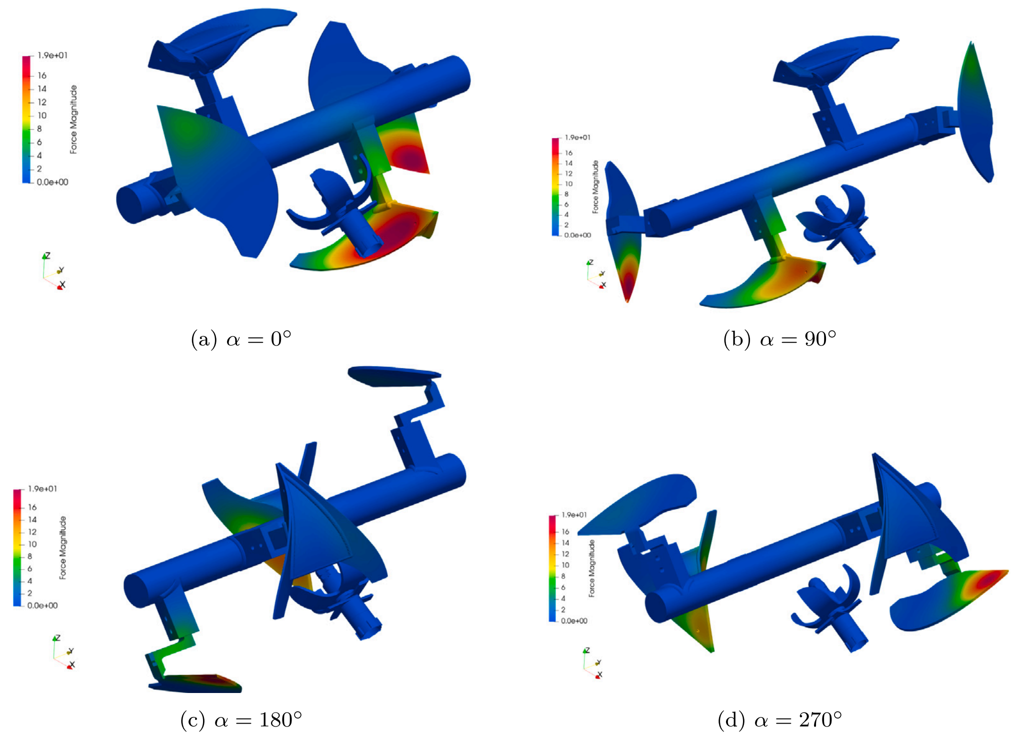

Fig. 20. Force on plowshares and scrapers in different shaft angles.

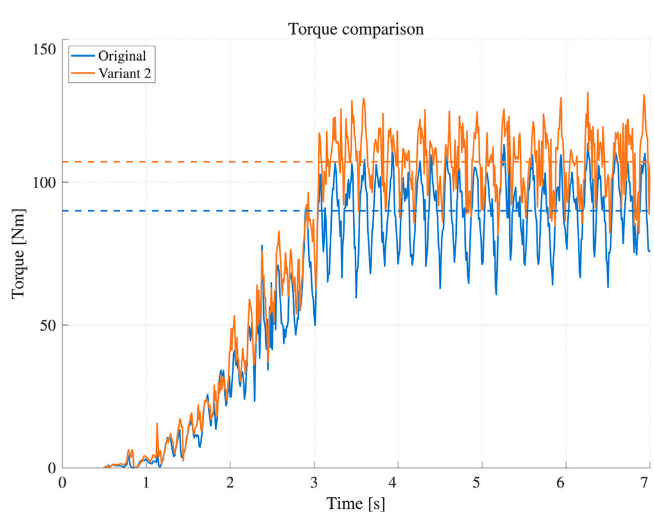

Fig. 21. Comparison of torque on the mixer shaft with different plowshare geometries.

for the shaft to reach its nominal angular velocity. This is due to the fact that, in this simulation, particles take approximately 3 s to fall from the hopper and enter the mixing chamber; thus, the mixer is not fully loaded before 3 s. Additionally, the torque profile exhibits a periodic pattern with a frequency twice that of the rotational speed. The torque peaks correspond to when one of the plowshares reaches the bottom of the mixing chamber.

The increase in torque associated with the modified plowshare is substantial and must be considered in practical applications. In this context, the modified geometry necessitates approximately 19% greater torque than the original. This result is consistent with simplified single-plowshare simulations, where the modified shape interacted more strongly with the material and promoted more intense lateral particle displacement. While this stronger interaction is beneficial for particle transport in the full-scale mixer, it also increases the mechanical load transmitted to the shaft.

The overall mixing quality was quantified by means of the Lacey index. For a binary mixture, let ϕ_m denote the global volume fraction of the reference component in the whole batch, namely

$$\phi_m = \frac{V_A}{V_A + V_B} \tag{5}$$

where V_A and V_B are the total particle volumes of the two components in the full simulated system. In the present work, ϕ_m was evaluated using all particles in the batch, including those still remaining in the hopper during the transient. This choice provides a stable global reference composition during the transient filling stage.

The mixing chamber was discretized into cubic control volumes (voxels) with sides 50 mm long, and for each occupied voxel i, the local volume fraction of the reference component was computed as

$$\phi_i = \frac{V_{A,i}}{V_{A,i} + V_{B,i}} \tag{6}$$

where $V_{A,i}$ and $V_{B,i}$ denote the volumes of the two components contained in voxel i.

Since the hopper does not constitute part of the actual mixing region, the variance term of the Lacey index was evaluated exclusively for the voxels corresponding to the mixing chamber. Furthermore, the variance calculation was weighted according to the particle-occupied volume in each voxel, thereby reducing the impact of sparsely populated voxels relative to densely filled ones [51,52]. The resultant

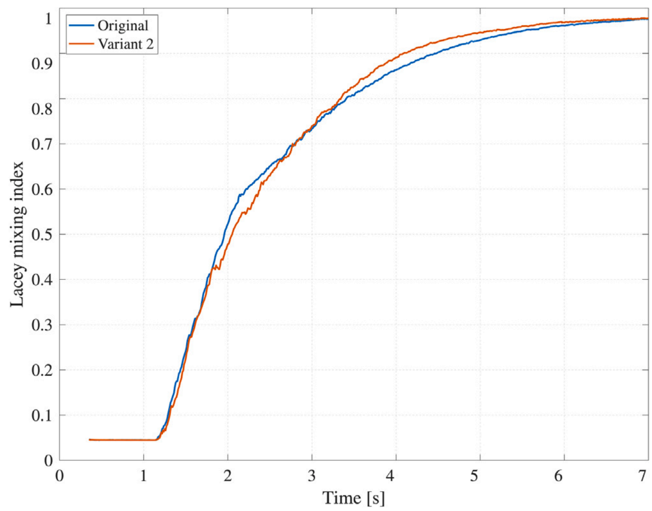

Fig. 22. Comparison of the Lacey index obtained with the original and modified plowshares.

variance was thus computed as:

$$S^2 = \frac{\sum_i V_i \left(\phi_i - \phi_m\right)^2}{\sum_i V_i} \tag{7}$$

where $V_i = V_{A,i} + V_{B,i}$ represents the total particle volume within voxel i, and the summation is restricted to occupied voxels within the mixing chamber.

The variance associated with a completely segregated mixture is defined as

$$S_0^2 = \phi_m(1 - \phi_m) \tag{8}$$

Conversely, the variance corresponding to a fully random mixture was estimated as

$$S_r^2 = \frac{S_0^2}{N} \tag{9}$$

where N denotes the total number of particles present in the mixing chamber.

Finally, the Lacey index was computed as

$$M = \frac{S_0^2 - S^2}{S_0^2 - S_r^2} \tag{10}$$

with $M = 0$ corresponding to complete segregation and $M = 1$ to an ideally random mixture.

Fig. 22 presents the temporal evolution of the Lacey index for both the original and modified plowshare geometries. Both designs result in a rapid post-filling increase in the mixing index, ultimately attaining high values that indicate effective mixing of the powders within the chamber. The Lacey index obtained with the original plowshares at $t = 7$ s is $M = 0.9773$, and the one obtained with the modified plowshare is $M = 0.9779$. The modified plowshare achieves marginally higher Lacey index values; however, the difference relative to the original geometry remains minimal. Thus, while the modified plowshare enhances the convective transport mechanism observed in simplified simulations, this improvement translates to only a slight increase in the global mixing index in the full-scale scenario. While Table 3 indicates improved lateral transport efficiency at the single-plowshare level, the full-scale simulations show that this advantage does not translate into a significant improvement of the global mixing index.

When the Lacey index approaches unity, further improvements are inherently challenging. Nonetheless, the practical relevance of such gains must be evaluated considering also the corresponding mechanical costs. In this investigation, the marginal increase in mixing quality associated with the modified plowshare comes at the expense of a substantially higher torque requirement. Consequently, while the modified geometry facilitates slightly faster and more advanced mixing, it does not offer an advantageous balance between mixing performance and mechanical load. Thus, the modified geometry should not be considered a universally superior solution, but rather a design that prioritizes mixing quality over mechanical efficiency.

6. Conclusion

This study has presented a DEM-based analysis of an industrial plowshare mixer, with particular emphasis on the relationships among particle transport mechanisms, plowshare geometry, and mechanical load. The DEM material models for baking soda and corn starch were calibrated and validated against experimental flow-function measurements, and their bulk behavior was further assessed through angle-of-repose simulations, demonstrating physically meaningful agreement with literature data. These steps established a robust foundation for the subsequent full-scale simulations of the mixer.

The simulations of the original mixer configuration enabled quantification of the force distribution on plowshares and scrapers, the corresponding shaft torque, and the baseline evolution of mixing quality. The results confirmed that the most significant interactions occur when the plowshares operate in the lower part of the chamber, where the greatest quantity of material is displaced. Additionally, the simulations elucidated the convective role of the plowshares and scrapers in preventing stagnant zones and in continually reintroducing powder into the active mixing region.

Building on these findings, a plowshare design strategy was proposed with a focus on lateral redirection of particles, identified as a critical transport mechanism for convective mixing. Simplified single-plowshare simulations were employed to isolate the geometric effects of the blade and to compare alternative shapes under controlled conditions. These simulations demonstrated that the modified geometry enhances lateral transport and strengthens the interaction with the powder bed. Moreover, this trend remained robust across variations in material rheology, indicating that the identified mechanism is not limited to a single powder model.

The revised full-scale simulations of the industrial mixer confirmed that the modified plowshare influences the mixing process in the anticipated manner. The corresponding Lacey index is marginally higher than that of the original plowshare at the end of the simulation interval, indicating that the modified geometry promotes somewhat faster and slightly more advanced mixing. However, this geometry also increases the torque required by the shaft from approximately 90 Nm to 107 Nm. Consequently, the full-scale analysis demonstrates that the modified plowshare does not yield a favorable overall trade-off between mixing quality and mechanical load.

The main conclusion of this work is therefore twofold. First, analyzing particle transport mechanisms provides an effective framework for understanding how plowshare geometry affects powder motion and local convective transport. Second, improvements in local transport mechanisms do not necessarily translate into practically advantageous designs at the scale of the full industrial mixer. In the present case, the modified plowshare yields only a marginal improvement in global mixing quality, while the associated increase in torque is considerably more substantial. The proposed methodology remains valuable as a design and analysis tool; however, the results underscore that enhancements in local transport must always be evaluated in conjunction with the full-scale energetic cost. Future research will address broader operating conditions, extended mixing times, and experimental evaluation of the geometries to determine whether more favorable trade-offs can be achieved.

Table A.6
Baking soda particle characteristics.

Particle characteristics		
Density	ρ	2200 kg/m^3
Shape	–	spherical
Radius	r	0.25 mm
Particle–particle interactions		
Young's modulus	E	520 kPa
Poisson's coefficient	ν	0.3
Coefficient of restitution	CoR	0.5
Static friction coefficient	μ_s	0.77
Rolling resistance coefficient	C_{rr}	0.3
Particle-steel interactions		
Coefficient of restitution	CoR	0.5
Wall friction coefficient	μ_w	0.37

Table A.7
Corn starch particle characteristics.

Particle characteristics		
Density	ρ	1450 kg/m^3
Shape	–	Clump shown in Fig. 6
Radius	r	0.85 mm
Particle–particle interactions		
Young's modulus	E	120 kPa
Poisson's coefficient	ν	0.3
Coefficient of restitution	CoR	0.3
Static friction coefficient	μ_s	0.85
Rolling resistance coefficient	C_{rr}	0.2
Particle-steel interactions		
Coefficient of restitution	CoR	0.3
Wall friction coefficient	μ_w	0.54

CRediT authorship contribution statement

Giovanni Bianchi: Writing – review & editing, Writing – original draft, Visualization, Validation, Software, Methodology, Investigation, Formal analysis, Data curation. **Giorgio Tagliavini:** Writing – review & editing, Visualization, Validation, Resources, Investigation, Data curation. **Andrea Marchetti:** Validation, Resources, Investigation. **Gianluca Panzacchi:** Supervision, Project administration. **Francesco Braghin:** Writing – review & editing, Supervision, Methodology, Funding acquisition, Conceptualization.

Funding sources

This work was supported financially by WAMGROUP.

Declaration of competing interest

The authors declare the following financial interests/personal relationships which may be considered as potential competing interests: Politecnico di Milano, Dipartimento di Meccanica reports financial support was provided by WAMGROUP. If there are other authors, they declare that they have no known competing financial interests or personal relationships that could have appeared to influence the work reported in this paper.

Acknowledgments

The authors sincerely thank WAMGROUP for the kind concession to publish the outcome of this research.

Appendix A. DEM parameters of baking soda and corn starch

See Tables A.6 and A.7.

Appendix B. Supplementary data

Supplementary material related to this article can be found online at https://doi.org/10.1016/j.powtec.2026.122780.

Data availability

No data was used for the research described in the article.

References

[1] F. Bertrand, L.-A. Leclaire, G. Levecque, DEM-based models for the mixing of granular materials, Chem. Eng. Sci. 60 (8) (2005) 2517–2531, http://dx.doi.org/10.1016/j.ces.2004.11.048, URL https://www.sciencedirect.com/science/article/pii/S0009250904009492. 5th International Symposium on Mixing in Industrial Processes (ISMIP5).

[2] S. Radl, E. Kalvoda, B.J. Glasser, J.G. Khinast, Mixing characteristics of wet granular matter in a bladed mixer, Powder Technol. 200 (3) (2010) 171–189, http://dx.doi.org/10.1016/j.powtec.2010.02.022, URL https://www.sciencedirect.com/science/article/pii/S0032591010000963.

[3] J. Bridgwater, Mixing of powders and granular materials by mechanical means—A perspective, Particuology 10 (4) (2012) 397–427, http://dx.doi.org/10.1016/j.partic.2012.06.002, URL https://www.sciencedirect.com/science/article/pii/S1674200112001149.

[4] S. Pantaleev, S. Yordanova, A. Janda, M. Marigo, J.Y. Ooi, An experimentally validated DEM study of powder mixing in a paddle blade mixer, Powder Technol. 311 (2017) 287–302, http://dx.doi.org/10.1016/j.powtec.2016.12.053, URL https://www.sciencedirect.com/science/article/pii/S0032591016309305.

[5] N. Salloum, T. Brinz, A. Atxutegi, S. Heinrich, Design and optimization of stirrer and mixer design for the correct mixing of pharmaceutical powders through DEM, Powder Technol. 449 (2025) 120413, http://dx.doi.org/10.1016/j.powtec.2024.120413, URL https://www.sciencedirect.com/science/article/pii/S003259102401057X.

[6] T.A. Simons, R. Weiler, S. Strege, S. Bensmann, M. Schilling, A. Kwade, A ring shear tester as calibration experiment for DEM simulations in agitated mixers – A sensitivity study, Procedia Eng. 102 (2015) 741–748, http://dx.doi.org/10.1016/j.proeng.2015.01.178, URL https://www.sciencedirect.com/science/article/pii/S1877705815001794. New Paradigm of Particle Science and Technology Proceedings of The 7th World Congress on Particle Technology.

[7] X. Gao, J. Yu, L. Lu, C. Li, W.A. Rogers, Development and validation of SuperDEM-CFD coupled model for simulating non-spherical particles hydrodynamics in fluidized beds, Chem. Eng. J. 420 (2021) 127654, http://dx.doi.org/10.1016/j.cej.2020.127654, URL https://www.sciencedirect.com/science/article/pii/S1385894720337761.

[8] G. Chandratilleke, A. Yu, J. Bridgwater, A DEM study of the mixing of particles induced by a flat blade, Chem. Eng. Sci. 79 (2012) 54–74, http://dx.doi.org/10.1016/j.ces.2012.05.010, URL https://www.sciencedirect.com/science/article/pii/S0009250912002849.

[9] B. Laurent, P. Cleary, Comparative study by PEPT and DEM for flow and mixing in a ploughshare mixer, Powder Technol. 228 (2012) 171–186, http://dx.doi.org/10.1016/j.powtec.2012.05.013, URL https://www.sciencedirect.com/science/article/pii/S0032591012003282.

[10] M. Marigo, M. Davies, T. Leadbeater, D. Cairns, A. Ingram, E. Stitt, Application of positron emission particle tracking (PEPT) to validate a discrete element method (DEM) model of granular flow and mixing in the turbula mixer, Int. J. Pharm. 446 (1) (2013) 46–58, http://dx.doi.org/10.1016/j.ijpharm.2013.01.030, URL https://www.sciencedirect.com/science/article/pii/S0378517313000616.

[11] R. Liu, X. Yin, H. Li, Q. Shao, P. York, Y. He, T. Xiao, J. Zhang, Visualization and quantitative profiling of mixing and segregation of granules using synchrotron radiation X-ray microtomography and three dimensional reconstruction, Int. J. Pharm. 445 (1) (2013) 125–133, http://dx.doi.org/10.1016/j.ijpharm.2013.02.010, URL https://www.sciencedirect.com/science/article/pii/S0378517313001440.

[12] S.L. Conway, A. Lekhal, J.G. Khinast, B.J. Glasser, Granular flow and segregation in a four-bladed mixer, Chem. Eng. Sci. 60 (24) (2005) 7091–7107, http://dx.doi.org/10.1016/j.ces.2005.03.008, URL https://www.sciencedirect.com/science/article/pii/S0009250905002150.

[13] E. Alizadeh, F. Bertrand, J. Chaouki, Discrete element simulation of particle mixing and segregation in a tetrapodal blender, Comput. Chem. Eng. 64 (2014) 1–12, http://dx.doi.org/10.1016/j.compchemeng.2013.12.009, URL https://www.sciencedirect.com/science/article/pii/S0098135413003906.

[14] H. Kuo, P. Knight, D. Parker, Y. Tsuji, M. Adams, J. Seville, The influence of DEM simulation parameters on the particle behaviour in a V-mixer, Chem. Eng. Sci. 57 (17) (2002) 3621–3638, http://dx.doi.org/10.1016/S0009-2509(02)00086-6, URL https://www.sciencedirect.com/science/article/pii/S0009250902000866.

[15] M. Pezo, L. Pezo, A. Jovanović, B. Lončar, R. Čolović, DEM/CFD approach for modeling granular flow in the revolving static mixer, Chem. Eng. Res. Des. 109 (2016) 317–326, http://dx.doi.org/10.1016/j.cherd.2016.02.003, URL https://www.sciencedirect.com/science/article/pii/S0263876216000666.

[16] Q. Hou, K. Dong, A. Yu, DEM study of the flow of cohesive particles in a screw feeder, Powder Technol. 256 (2014) 529–539, http://dx.doi.org/10.1016/j.powtec.2014.01.062, URL https://www.sciencedirect.com/science/article/pii/S0032591014000710.

[17] L. Pezo, A. Jovanović, M. Pezo, R. Čolović, B. Lončar, Modified screw conveyor-mixers – discrete element modeling approach, Adv. Powder Technol. 26 (5) (2015) 1391–1399, http://dx.doi.org/10.1016/j.apt.2015.07.016, URL https://www.sciencedirect.com/science/article/pii/S0921883115001594.

[18] S. Golshan, R. Zarghami, H.R. Norouzi, N. Mostoufi, Granular mixing in nauta blenders, Powder Technol. 305 (2017) 279–288, http://dx.doi.org/10.1016/j.powtec.2016.09.059, URL https://www.sciencedirect.com/science/article/pii/S003259101630643X.

[19] P. Liu, R. Yang, A. Yu, DEM study of the transverse mixing of wet particles in rotating drums, Chem. Eng. Sci. 86 (2013) 99–107, http://dx.doi.org/10.1016/j.ces.2012.06.015, URL https://www.sciencedirect.com/science/article/pii/S0009250912003648. 5th International Granulation Workshop.

[20] M. Yamamoto, S. Ishihara, J. Kano, Evaluation of particle density effect for mixing behavior in a rotating drum mixer by DEM simulation, Adv. Powder Technol. 27 (3) (2016) 864–870, http://dx.doi.org/10.1016/j.apt.2015.12.013, URL https://www.sciencedirect.com/science/article/pii/S0921883115002769. Special issue of the 5th Int'l Conf. on the Characterization and Control of Interfaces for High Quality Advanced Materials (ICCCI2015).

[21] H. Norouzi, R. Zarghami, N. Mostoufi, Insights into the granular flow in rotating drums, Chem. Eng. Res. Des. 102 (2015) 12–25, http://dx.doi.org/10.1016/j.cherd.2015.06.010, URL https://www.sciencedirect.com/science/article/pii/S0263876215002154.

[22] X. Hua, J. Curtis, B. Hancock, W. Ketterhagen, C. Wassgren, The kinematics of non-cohesive, sphero-cylindrical particles in a low-speed, vertical axis mixer, Chem. Eng. Sci. 101 (2013) 144–164, http://dx.doi.org/10.1016/j.ces.2013.05.063, URL https://www.sciencedirect.com/science/article/pii/S000925091300403X.

[23] M. Alian, F. Ein-Mozaffari, S.R. Upreti, Analysis of the mixing of solid particles in a plowshare mixer via discrete element method (DEM), Powder Technol. 274 (2015) 77–87, http://dx.doi.org/10.1016/j.powtec.2015.01.012, URL https://www.sciencedirect.com/science/article/pii/S0032591015000224.

[24] A. Hassanpour, H. Tan, A. Bayly, P. Gopalkrishnan, B. Ng, M. Ghadiri, Analysis of particle motion in a paddle mixer using discrete element method (DEM), Powder Technol. 206 (1) (2011) 189–194, http://dx.doi.org/10.1016/j.powtec.2010.07.025, URL https://www.sciencedirect.com/science/article/pii/S0032591010003724. 9th International Symposium on Agglomeration and 4th International Granulation Workshop, 2009.

[25] Y. Tsugeno, M. Sakai, S. Yamazaki, T. Nishinomiya, DEM simulation for optimal design of powder mixing in a ribbon mixer, Adv. Powder Technol. 32 (5) (2021) 1735–1749, http://dx.doi.org/10.1016/j.apt.2021.03.026, URL https://www.sciencedirect.com/science/article/pii/S092188312100159X.

[26] J. Nečas, J. Rozbroj, J. Hlosta, J. Diviš, J. Kaprálek, D. Žurovec, J. Zegzulka, Shear lid motion in DEM shear calibration and the effect of particle rearrangement on the internal friction angle, Powder Technol. 403 (2022) 117417, http://dx.doi.org/10.1016/j.powtec.2022.117417, URL https://www.sciencedirect.com/science/article/pii/S0032591022003114.

[27] O. Baran, A. DeGennaro, E. Ramé, A. Wilkinson, DEM simulation of a schulze ring shear tester, AIP Conf. Proc. 1145 (1) (2009) 409–412, http://dx.doi.org/10.1063/1.3179948, URL https://doi.org/10.1063/1.3179948.

[28] M.J. Mohajeri, H.Q. Do, D.L. Schott, DEM calibration of cohesive material in the ring shear test by applying a genetic algorithm framework, Adv. Powder Technol. 31 (5) (2020) 1838–1850, http://dx.doi.org/10.1016/j.apt.2020.02.019, URL https://www.sciencedirect.com/science/article/pii/S0921883120300716.

[29] P.W. Cleary, J.E. Hilton, M.D. Sinnott, Modelling of industrial particle and multiphase flows, Powder Technol. 314 (2017) 232–252, http://dx.doi.org/10.1016/j.powtec.2016.10.072, URL https://www.sciencedirect.com/science/article/pii/S0032591016307653. Special Issue on Simulation and Modelling of Particulate Systems.

[30] Z. Fang, S. Peng, J. Yi, J. Du, Structure optimization of ploughblades in a ploughshare mixer using the DEM simulations, Eng. Comput. 37 (9) (2020) 3455–3475, http://dx.doi.org/10.1108/EC-01-2020-0032.

[31] J.F. Labuz, A. Zang, Mohr–Coulomb failure criterion, Comput. Phys. Comm. 45 (2012) 975–979, http://dx.doi.org/10.1007/s00603-012-0281-7.

[32] D. Schulze, Powders and Bulk Solids, Springer Berlin, Heidelberg, 2008, http://dx.doi.org/10.1007/978-3-540-73768-1.

[33] ASTM International, Standard Test Method for Bulk Solids Using Schulze Ring Shear Tester, Standard D6773-16, ASTM International, West Conshohocken, PA, 2016, http://dx.doi.org/10.1520/D6773-16, URL www.astm.org.

[34] ASTM International, Standard Test Method for Measuring the Shear Stresses of Powders Using the Peschl Rotational Split Level Shear Tester, Standard D6682-01, ASTM International, West Conshohocken, PA, 2001, http://dx.doi.org/10.1520/D6682-01, URL www.astm.org.

[35] ASTM International, Standard Test Method for Shear Testing of Bulk Solids Using the Jenike Shear Tester, Standard D6128-16, ASTM International, West Conshohocken, PA, 2016, http://dx.doi.org/10.1520/D6128-16, URL www.astm.org.

[36] Z. Yan, S.K. Wilkinson, E.H. Stitt, M. Marigo, Discrete element modelling (DEM) input parameters: understanding their impact on model predictions using statistical analysis, Comput. Part. Mech. 2 (2015) 283–299, http://dx.doi.org/10.1007/s40571-015-0056-5.

[37] H. Chen, Y. Xiao, Y. Liu, Y. Shi, Effect of Young's modulus on DEM results regarding transverse mixing of particles within a rotating drum, Powder Technol. 318 (2017) 507–517, http://dx.doi.org/10.1016/j.powtec.2017.05.047, URL https://www.sciencedirect.com/science/article/pii/S0032591017304540.

[38] J. Hlosta, L. Jezerská, J. Rozbroj, D. Žurovec, J. Nečas, J. Zegzulka, DEM investigation of the influence of particulate properties and operating conditions on the mixing process in rotary drums: Part 1—Determination of the DEM parameters and calibration process, Processes 8 (2) (2020) http://dx.doi.org/10.3390/pr8020222, URL https://www.mdpi.com/2227-9717/8/2/222.

[39] S. Lommen, D. Schott, G. Lodewijks, DEM speedup: Stiffness effects on behavior of bulk material, Particuology 12 (2014) 107–112, http://dx.doi.org/10.1016/j.partic.2013.03.006, URL https://www.sciencedirect.com/science/article/pii/S1674200113001387. Special issue on conveying and handling of particulate solids – Challenges of discrete element simulation, application and calibration.

[40] N. Meyer, E.L. Wagemann, A. Jackstadt, R. Seifried, Material and particle size sensitivity analysis on coefficient of restitution in low-velocity normal impacts, Comput. Part. Mech. 9 (2022) 1293–1308, http://dx.doi.org/10.1007/s40571-022-00471-z.

[41] P. Aela, L. Zong, Z.-Y. Yin, M. Esmaeili, G. Jing, Calibration method for discrete element modeling of ballast particles, Comput. Part. Mech. 10 (2023) 481–493, http://dx.doi.org/10.1007/s40571-022-00507-4.

[42] H.S. Elmsahli, I.C. Sinka, A discrete element study of the effect of particle shape on packing density of fine and cohesive powders, Comput. Part. Mech. 8 (2021) 183–200, http://dx.doi.org/10.1007/s40571-020-00322-9.

[43] K. Iwashita, M. Oda, Rolling resistance at contacts in simulation of shear band development by DEM, J. Eng. Mech. 124 (3) (1998) 285–292, http://dx.doi.org/10.1061/(ASCE)0733-9399(1998)124:3(285).

[44] R. Zhang, B. Tagliafierro, C. Vanden Heuvel, S. Sabarwal, L. Bakke, Y. Yue, X. Wei, R. Serban, D. Negruţ, Chrono DEM-engine: A discrete element method dual-GPU simulator with customizable contact forces and element shape, Comput. Phys. Comm. 300 (2024) 109196, http://dx.doi.org/10.1016/j.cpc.2024.109196, URL https://www.sciencedirect.com/science/article/pii/S001046552400119X.

[45] J.F. Nunes, F.C.A. de Alcântara, V.A. da Silva Moris, S.C. dos Santos Rocha, Fluid dynamics and coating of sodium bicarbonate in a vibrofluidized bed, Chem. Eng. Process.: Process. Intensif. 52 (2012) 34–40, http://dx.doi.org/10.1016/j.cep.2011.12.003, URL https://www.sciencedirect.com/science/article/pii/S0255270111002583.

[46] J. Chen, X. Wang, Y. Chi, S. Guo, Y. Cao, H. Chen, S. Wu, J. Gong, Controllable preparation of monodisperse spherical sodium bicarbonate particles with stable dissolution performance and good powder properties, Powder Technol. 453 (2025) 120683, http://dx.doi.org/10.1016/j.powtec.2025.120683, URL https://www.sciencedirect.com/science/article/pii/S0032591025000786.

[47] J. Yang, A. Sliva, A. Banerjee, R.N. Dave, R. Pfeffer, Dry particle coating for improving the flowability of cohesive powders, Powder Technol. 158 (1) (2005) 21–33, http://dx.doi.org/10.1016/j.powtec.2005.04.032, URL https://www.sciencedirect.com/science/article/pii/S0032591005001531. Prof. Dr.-Ing. Otto Molerus 70th birthday.

[48] R. Davé, S. Kim, K. Kunnath, S. Tripathi, A concise treatise on model-based enhancements of cohesive powder properties via dry particle coating, Adv. Powder Technol. 33 (11) (2022) 103836, http://dx.doi.org/10.1016/j.apt.2022.103836, URL https://www.sciencedirect.com/science/article/pii/S0921883122004150.

[49] M. Stasiak, M. Molenda, I. Opalinski, W. Blaszczak, Mechanical properties of native maize, wheat, and potato starches, Czech J. Food Sci. 31 (4) (2013) 347–354, http://dx.doi.org/10.17221/348/2012-CJFS.

[50] Roquette, Powdered NF corn starch, 2026, https://www.roquette.com/health-pharma/pharmaceutical-product-catalog/powder-nf-corn-starch#informations. (Accessed 22 April 2026).

[51] M. Jiang, Y. Zhao, G. Liu, J. Zheng, Enhancing mixing of particles by baffles in a rotating drum mixer, Particuology 9 (3) (2011) 270–278, http://dx.doi.org/10.1016/j.partic.2010.06.008, URL https://www.sciencedirect.com/science/article/pii/S1674200111000332.

[52] V.D. Chung, F. Radjai, Effect of particle density on powder mixing in nuclear fuel pellet fabrication using discrete element method, J. Sci. Technol. Civ. Eng. (JSTCE) - HUCE 19 (4) (2025) 18–28, http://dx.doi.org/10.31814/stce.huce2025-19(4)-02, URL https://stce.huce.edu.vn/index.php/en/article/view/3295.